



**Large Polaron Formation and its Effect on Electron
Transport in Hybrid Perovskite**

Journal:	<i>Energy & Environmental Science</i>
Manuscript ID	EE-COM-11-2018-003369.R1
Article Type:	Communication
Date Submitted by the Author:	29-Jan-2019
Complete List of Authors:	Zheng, Fan; E O Lawrence Berkeley National Laboratory, Wang, Lin-Wang; Lawrence Berkeley National Laboratory,

Large Polaron Formation and its Effect on Electron Transport in Hybrid Perovskite

Fan Zheng and Lin-wang Wang*

Joint Center for Artificial Photosynthesis and Materials Sciences Division, Lawrence Berkeley National Laboratory, Berkeley, California 94720, USA.

E-mail: lwwang@lbl.gov

Abstract

Many experiments have indicated that large polaron may be formed in hybrid perovskite, and its existence is proposed to screen the carrier-carrier and carrier-defect scattering, thus contributing to the long lifetime for the carriers. However, detailed theoretical study of the large polaron and its effect on carrier transport at the atomic level is still lacking. In particular, how strong is the large polaron binding energy, how does its effect compare with the effect of dynamic disorder caused by the *A*-site molecular rotation, and how does the inorganic sublattice vibration impact the motion of the large polaron, all these questions are largely unanswered. In this work, using $\text{CH}_3\text{NH}_3\text{PbI}_3$ as an example, we implement tight-binding model fitted from the density-functional theory to describe the electron large polaron ground state and to understand the large polaron formation and transport at its strong-coupling limit. We find that the formation energy of the large polaron is around -12 meV for the case without dynamic disorder, and -55 meV by including dynamic disorder. By performing the explicit time-dependent wavefunction evolution of the polaron state, together with the rotations of CH_3NH_3^+ and vibrations of PbI_3^- sublattice, we studied the diffusion constant and mobility of the large polaron state driven by the dynamic disorder

19 and the sublattice vibration. Two effects of the inorganic sublattice vibration are
20 found: on one hand, the vibration of the sublattice provides additional driving force
21 for carrier mobility, on the other hand, the large polaron polarization further localizes
22 the electron, reducing its mobility. Overall, the effect of the large polaron is to slow
23 down the electron mobility by roughly a factor of two. We believe that both dynamic
24 disorder due to rotation of the organic molecule, and large polaron effects induced by
25 the polarization and vibration of the inorganic sublattice, play important roles for the
26 electronic structure and carrier dynamics of the system.

Broader Context

Hybrid perovskite has attracted a great deal of research interest, not only because of its high power conversion efficiency for solar cells, but also because the intrinsic new physics exists in the system. In particular, the interplays between the *A*-site molecular reorientation, soft lattice vibration and electron localization have produced novel physical phenomena different from conventional semiconductors. Many investigations have demonstrated the localization of the excited carriers caused by the fast rotation of *A*-site molecules (dynamic disorder). Meanwhile, other works have shown the strong electron-phonon coupling, hypothesizing the formation of large polaron. However, an *ab initio* treatment including both dynamic disorder and large polaron is difficult, and the role of the large polaron in such localized electron system is still unclear. In this work, by using large-scale *ab initio* derived tight-binding model, we have directly simulated the effect of the large polaron and the resulting electron diffusion. We have included both lattice screening and dynamic disorder at equal footing. In addition to the screening, the lattice vibrational contribution to the electron diffusion is also incorporated. Such model offers a clear understanding of the contributions to the carrier motion due to different effects, and lays the groundwork to study the general large polaron formation and transport in hybrid perovskites.

27 *Introduction.* The outstanding performance of hybrid perovskites (HPs) as the solar cell
28 has attracted a great number of studies to understand its fundamental physical principles.
29 In addition to its high tolerance for defects,¹⁻⁴ the exceptionally long carrier lifetime and
30 diffusion length despite the modest mobility for the excited carriers, have become the mostly
31 focused research topic.⁵⁻⁹ Many mechanisms have been proposed to explain such long carrier
32 lifetime and diffusion length. For example, owing to the dipole moment of the molecules such
33 as CH_3NH_3^+ (MA), it has been hypothesized that the polar nature of the molecule introduces
34 the ferroelectricity and polar potential in HPs.¹⁰ It has also been proposed that ferroelectric
35 domain and domain walls contribute to the fast electron-hole separation and slow recombi-
36 nation.¹¹⁻¹⁴ Besides, the broken inversion symmetry can also lead to the so-called Rashba
37 effect under the strong spin-orbit coupling introduced by heavy atoms such as Pb and I. The
38 different spin chiralities and the momentum vectors of the band edge states with spin and
39 momentum mismatch forbid the carrier-recombination in k space,¹⁵⁻¹⁸ prolonging the life-
40 time of the excited carriers. However, the ferroelectricity of HPs has been under debate,^{19,20}
41 as many works show that this material could be centrosymmetric at room temperature ow-
42 ing to the fast reorientation of the molecules. In addition, pure inorganic halide perovskite
43 CsPbX_3 also shows similar carrier behavior to the hybrid case.^{21,22} Instead of forming ferro-
44 electric domain, another explanation based on the dipole moment of the MA is the dynamic
45 disorder, where the disordered orientation of the molecules exhibit random potential on in-
46 organic sublattice such as PbI_3^- . Such varying potential modulates the band edge states
47 of the electrons and holes, and produces spatially localized wavefunctions at different loca-
48 tions on a nano-size scale in real space,²³⁻²⁶ which suppresses their recombination. Recently,
49 more has been found that both the fast-rotating molecules and the soft inorganic sublattice
50 can affect the carrier transport via the strong electron-phonon coupling.^{15,27-29} Compared to
51 conventional direct-band-gap semiconductors such as GaAs, the modest carrier mobility of
52 MAPbI_3 indicates the contribution to the carrier scattering by optical phonon modes.^{9,30,31}
53 It is believed that with the relatively strong electron-phonon coupling, the large polaron can

54 be formed to develop the pseudo-free dressed carriers, and it can screen them from other
55 carriers and defects to avoid recombination and trapping, which leads to long lifetime and
56 long diffusion length.^{32–36}

57 Large polaron refers to the shallow bound state due to Coulomb interaction between the
58 charge carrier and the polarizable lattice. The so-called small polaron has been studied in
59 this material, where the wavefunction is strongly localized within chemical bonds.^{35–37} It
60 is believed that the *A*-site molecules play a significant role in forming the small polarons,
61 and such small polaron is crucial to explain the formation and annihilation of the trap
62 states. However, different from the small polarons, large polaron often spreads over hun-
63 dreds of unit cells owing to the relatively weak long-range Coulomb interaction and small
64 lattice distortion by the longitudinal optical (LO) phonon mode.³⁸ It is suggested that the
65 long time decay of more than 100 ps for the hot carrier relaxation in the experiments for
66 various HPs,^{7,39–41} could be owing to the large polaron screening^{39,40,42} (at low excitation
67 density) or the “phonon bottleneck” (at high excitation density caused by the large polaron
68 overlapping).^{27,43,44} The Fröhlich model further reveals the size of the large polaron and its
69 transport estimated from model Hamiltonian.²⁷ Using the time-resolved optical Kerr effect
70 spectroscopy, the large polaron formation time is estimated to be around 0.3ps to 0.7ps
71 in MAPbBr₃ and CsPbBr₃.⁴⁵ A pioneer first-principle’s calculation with hybrid exchange-
72 correlation functional has shown the possible formations of large polarons in CsPbBr₃ and
73 MAPbBr₃ along one direction, and has estimated their formation energies to be 140 and
74 60 meV, respectively.⁴⁶ In this calculation, it is observed that PbBr₃[−] lattice deforms under
75 the charge of an electron or hole.⁴⁶ Due to the large computational cost, the first-principle
76 calculation was only done for one dimensional polaron, instead of the real three dimensional
77 case. Owing to the possibility of overestimation of wavefunction delocalization with LDA
78 or GGA semi-local functional, direct density function theory (DFT) total energy calculation
79 must be dealt with carefully to avoid self-interaction errors. Furthermore, the previous *ab*
80 *initio* works only considered the static large polaron effect, without its coupling to the MA

81 molecular rotation, or sublattice vibration. As mentioned earlier, it has been experimentally
82 confirmed that the MA molecules are randomly re-orientating in a sub-picosecond time scale.
83 In our previous work,²⁴ we have shown that the random orientation of MA cause random
84 potentials, which can localize the electrons and holes at different locations in real space and
85 reduce their recombination. The rotation of MA also induces a dynamic disorder changing
86 with time, providing a driving force for the carrier motion. Time-dependent Schrödinger's
87 equation following the fluctuating potentials yields a carrier mobility, which agrees with the
88 experimental value within its uncertainty range. However, in our previous work, the effects
89 of the PbI_3^- inorganic sublattice has not been included. This sublattice has two additional
90 potential effects, one is the large polaron bound polarization potential which further localizes
91 the carrier wavefunction, another is the fluctuation of the lattice which provides additional
92 driving force for the carrier movement.

93 In this work, we include the large polaron effect together with the dynamic disorder
94 provided by the MA rotations and the vibrations of the PbI_3^- sublattice. Since the large
95 polaron effect is caused by Coulomb interaction between the charge carrier and the lattice
96 optical phonons, we construct a tight-binding (TB) model of MAPbI_3 ¹⁵ following from DFT
97 calculations. As shown previously,²⁴ such TB model can describe the carrier localization
98 accurately, reproducing the large-scale DFT calculation results for tens of thousands of
99 atoms. The formation of the polaron as well as its dynamics under the influence of the
100 MA rotation and PbI_3^- sublattice vibration is simulated directly with a $48 \times 48 \times 48$ supercell
101 system with more than 1 million atoms. Our directly calculated formation energy agrees
102 with the Fröhlich model within the strong coupling approximation. Since the temperature
103 directly influences the rate of the molecular rotation, we compute the diffusion constant of
104 the electron at different molecular re-orientation rates and with different PbI_3^- sublattice
105 vibrations at different temperatures. The effect of PbI_3^- sublattice vibration is modeled with
106 the molecular dynamics of the sublattice, which alters the TB model coupling parameters
107 and on-site potentials. Our calculation suggests that the mobility of the electron is reduced

108 by a factor of 2 by including the polaron and sublattice vibrational effects. However, adding
109 vibrational effect of the PbI_5^- sublattice tends to enhance the carrier diffusion more at high
110 temperature than at low temperature. The resulting mobility are within the experimental
111 uncertainty when compared with experimental values. By assuming a small activation energy
112 for the molecular reorientation rate, we obtain the same trend of the mobility with respect
113 to the temperature dependence as the experimental results.

114 *Large Polaron Formation.* A large polaron in a polarizable crystal is a result of two
115 competing factors. On one hand, the localization of a carrier wavefunction causes a posi-
116 tive kinetic energy scaling as $1/L^2$ where L is the size of the localized state. On the other
117 hand, such localized charge will induce the screening of the polarizable crystal lattice, result-
118 ing in a negative energy due to charge-polarization interaction scaling as $-1/L$. Note that
119 it is important to avoid the erroneous self-interaction possibly exist in DFT total energy
120 calculation which also scales as $1/L$. In DFT, the exact-exchange shall be used to cancel
121 the self-interaction error originated from Coulomb energy. An incomplete cancellation (if
122 using GGA or LDA) tends to yield a more extended polaron state. However, TB model
123 used here does not have Coulomb interaction term, thus no self-interaction error. Without
124 this self-interaction error, for sufficiently large L , the negative polarization energy will win
125 and the total energy could be lowered compared to the delocalized Bloch state. Therefore,
126 a large polaron can always be formed in a polarizable crystal, although its binding energy
127 may be smaller than the room temperature thermal energy, making it hard to observe. The
128 most popular large polaron Hamiltonian is proposed by Fröhlich, where the LO phonon
129 model is assumed to couple to the electron wavefunction.⁴⁷ The exact Fröhlich model is diffi-
130 cult to solve due to correlation effect.³⁸ However, under the strong-coupling approximation,
131 the large polaron wavefunction can be written as a product of the “electron” part and the
132 “ionic” part under the Born-Oppenheimer (BO) approximation. Under this approximation,
133 the total energy of the polaron is obtained by minimizing Eq.1 through variation of electron
134 wavefunction ψ :

$$\begin{aligned}
 E &= \langle \psi | H_0 | \psi \rangle - E^{\text{P}} \\
 E^{\text{P}} &= \frac{1}{2\bar{\epsilon}} \int d\mathbf{r} V^{\text{P}}(\mathbf{r}) \rho(\mathbf{r})
 \end{aligned}
 \tag{1}$$

135 where H_0 is the Hamiltonian of the electron without polaron effect, $\rho(\mathbf{r}) = |\psi(\mathbf{r})|^2$ is the
 136 charge density for state $\psi(\mathbf{r})$, E^{P} indicates the screening energy, and V^{P} is the polarization
 137 potential of the lattice in response to the Coulomb potential of $\rho(\mathbf{r})$. The screening caused
 138 by electron-phonon coupling consisting of the ionic contribution of the dielectric constant is
 139 represented by $\bar{\epsilon}$: $\frac{1}{\bar{\epsilon}} = \frac{1}{\epsilon_{\infty}} - \frac{1}{\epsilon_0}$. ϵ_{∞} and ϵ_0 are the electronic and static dielectric constants.
 140 Using DFT linear response theory,^{48–53} we have calculated ϵ_{∞} as 4.5, and ϵ_0 as 21. When
 141 the electron wavefunction is self-trapped in real space, it induces a distortion of the lattice to
 142 provide a polarization potential, which self-consistently localizes the electron wavefunction.
 143 Here, by expressing the electron energy with $\langle \psi | H_0 | \psi \rangle$, we avoid the self-interaction energy
 144 error. On the other hand, the screening of ψ due to other electron is represented by the
 145 ϵ_{∞} in the expression of $\bar{\epsilon}$. By minimizing the total energy of Eq. 1 with respect to the
 146 wavefunction, we obtain the Hamiltonian:

$$H |\psi\rangle = \left(H_0 - \frac{1}{\bar{\epsilon}} V^{\text{P}}[\rho] \right) |\psi\rangle = \epsilon |\psi\rangle
 \tag{2}$$

147 where V^{P} depends on the charge density ρ as $V^{\text{P}}(\mathbf{r}) = \int d\mathbf{r}' \frac{\rho(\mathbf{r}')}{|\mathbf{r}-\mathbf{r}'|}$. To achieve self-consistency,
 148 an iterative scheme is used to solve the Hamiltonian by updating the wavefunction and
 149 polarization potential for every iteration. Since the electron charge density ρ is localized in a
 150 relatively large area (e.g. 50 Å), a macroscopic dielectric constant $\bar{\epsilon}$ can be used to describe
 151 its screening effect.

152 Due to the large size of large polarons, we use a supercell of 48×48×48 (corresponding
 153 to more than 300 Å lattice), which is large enough to model polaron and its transport.

154 Apparently, such large system is beyond the reach of DFT. Since we are only interested in
 155 the conduction band edge for the electron, a tight-binding (TB) model with nearest-neighbor
 156 hopping is used to construct a Hamiltonian (see Supplementary Information (SI)).¹⁵ In this
 157 TB model, the onsite energy and hopping magnitude are fitted to the DFT calculated band
 158 structures. The TB parameters are listed in SI. These fitted parameters are also consistent
 159 with the Hamiltonian obtained using the maximally-localized Wannier function represen-
 160 tation.⁵⁴ Here, owing to its significance to the electronic structure,^{16,55,56} the spin-orbit
 161 coupling (SOC) is also included in the TB model⁵⁷ and the DFT calculations. As one can
 162 see in Fig.S1 of SI, the TB model reproduces well the DFT band edge electronic structures.
 163 Due to the sparse nature of the TB Hamiltonian, the parallelized ARPACK⁵⁸ math library
 164 is used to solve the eigen states. The ARPACK packages also allows us to solve the interior
 165 eigen states of the Hamiltonian. To solve Eq. 2 self-consistently, we start with a localized
 166 wavefunction ψ (for example, with an Gaussian-shape initial potential), iterate through the
 167 self-consistent equation until both kinetic energy ($\langle\psi|H_0|\psi\rangle$) and potential energy (E^P) are
 168 converged.

169 Fig. 1a shows the charge density of the large polaron state and its polarization potential
 170 $V^P/\bar{\epsilon}$ (Fig. 1b) when we ignore the dynamic disorder potential due to the random orientation
 171 of MA molecules. By comparing the energies with and without the large polaron effect, our
 172 TB calculation reveals the formation energy of the large polarons in such a crystal is about
 173 -12 meV. In Fröhlich model, a dimensionless coupling constant α is often used to quantify
 174 the electron-phonon coupling strength:

$$\alpha = \frac{e^2}{\hbar} \frac{1}{4\pi\epsilon} \left(\frac{1}{\epsilon_\infty} - \frac{1}{\epsilon_0} \right) \sqrt{\frac{m^*}{2\hbar\omega_{LO}}} \quad (3)$$

175 where ω_{LO} is the LO phonon frequency, and $m^* = 0.25$ is the effective mass of the electrons
 176 (or $m^* = 0.55$ for holes), fitted from the DFT band structure. Particularly, our phonon cal-

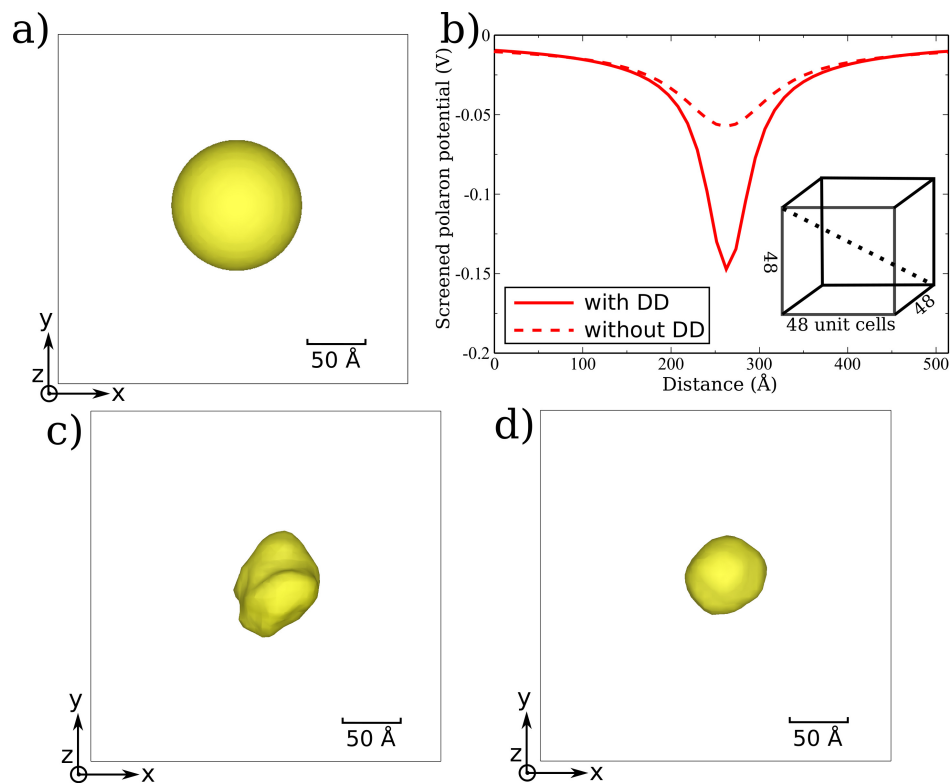


Figure 1: a) The conduction band minimum (CBM) state (charge density) with the large polaron effect (for clearness, all the atoms in this big supercell are not shown)
 . b) The screened polaron polarization potential $V^P/\bar{\epsilon}$ along the diagonal line of the cubic supercell (the diagonal line is shown in the inset diagram) for the case with and without dynamic disorder (DD) effect. c) The localized CBM state (charge density) induced by the DD without large polaron effect. d) The CBM state (charge density) under large polaron effect and DD. These states are plotted so that more than 85% charge is enclosed in the isosurface. The charge near the boundary of the supercell is negligible, showing that the size of the supercell is large enough.

177 culation and other work⁵⁹⁻⁶¹ show that there exist low energy LO phonons, corresponding to
 178 PbI_3^- sublattice vibrations. We average the phonon frequencies weighed by their contribution
 179 to the low-frequency dielectric constant, and acquire $\omega_{\text{LO}} = 2.39$ THz (SI). This value is con-
 180 sistent to both experimental²⁹ and theoretical^{62,63} work. Using this phonon frequency, the
 181 α is estimated as 3.24, which is in line with other halide ionic crystals such as CsI ($\alpha=3.67$),
 182 RbCl ($\alpha=3.81$) or oxide perovskite SiTiO_3 ($\alpha=3.77$).^{64,65} The large α of MAPbI_3 falls in the
 183 low end region of the strong coupling. This picture is further supported by the recent exper-
 184 iment report the formation of strong-coupling polaron in HP.⁶⁶ Within the strong-coupling
 185 approximation, the polaron formation energy can be computed as $E = -0.106\alpha^2\hbar\omega_{\text{LO}} = -11$
 186 meV,^{47,67} which agrees well with our direct TB modeling result. Here, the specific value of
 187 ω_{LO} does not influence the Fröhlich calculated binding energy, since it has been canceled
 188 in the above formula and Eq. 3. Meanwhile, the polaron state (charge density) can be
 189 fitted to a Gaussian function. Thus, if defining the size of the polaron as the deviation of
 190 the Gaussian function ($\bar{r} \equiv \sigma$), the radius of the polaron states obtained from TB model is
 191 estimated to be 28\AA . This is also consistent to 32\AA computed based on the Fröhlich model
 192 at strong-coupling limit with the Gaussian approximation.⁶⁷

193 As demonstrated in Ref. 24, the disordered MA molecular orientation produces potential
 194 variations on Pb and I atoms due to their dipole moments. Such random molecular potentials
 195 lead to the localized conduction band minimum (CBM) and valence band maximum (VBM)
 196 in the real space with nano-size scale as shown in Fig. 1c. This is a localized state before
 197 considering the large polaron effect, where the random potential is described inside H_0 . By
 198 adding the large polaron effect as the second term in Eq.1, it further localizes the charge
 199 shown in Fig. 1d. A polaron size around 50\AA has been obtained. Compared to the large
 200 polaron without dynamic disorder (Fig. 1a), the charge density is much more localized. It
 201 is also more localized compared to the case of dynamic disorder without large polaron effect
 202 (Fig. 1c). The solid line in Fig. 1b indicates the converged polarization potential along the
 203 diagonal line of the super cell for the large polaron state under the dynamic disorder. The

204 maximum amplitude of this potential is 0.15 eV, which is similar to the dynamic disorder
 205 potential fluctuation which is around 0.2 eV as shown in Fig. S4.²⁴ However, this potential
 206 is more narrow compared with the dynamic disorder potential fluctuation. The additional
 207 large polaron binding energy is about -55 meV. This binding energy is much larger than the
 208 -12 meV binding energy in the case without dynamic disorder. This is because the dynamic
 209 disorder already pre-localizes the electron wavefunction. Using this polarization potential,
 210 the spatial displacements of ions in generating such polarization could be estimated based
 211 on their Born-effective charge (SI). We estimate that such displacement is in average on the
 212 order of 0.001 Å, which is smaller than the thermal fluctuations around 0.01~0.1 Å.

213 *Polaron Transport.* In our previous work,²⁴ it is suggested that the transport of the
 214 excited electron is mainly driven by the molecular rotation induced dynamic disorder. When
 215 a molecule changes its orientation, its electric static potential on the neighboring Pb and I
 216 atoms is altered. The aforementioned localized CBM state can “hop” to a new state once
 217 its energy crosses with the energy of another state. In this work, in order to model such
 218 dynamical process with large polaron effect (i.e. the polarization screening effect due to the
 219 PbI_3^- sublattice), the Monte-Carlo (MC) simulation of the MA rotation is performed with
 220 a rotation rate taken from experimental measurement. For each MC step, the total energy
 221 difference is computed by summing over the screened dipole-dipole interactions between the
 222 molecules. This energy difference is used to accept or reject trial rotations. In our model,
 223 molecular dipoles are interacting with each other via the screened dipole-dipole interaction
 224 with the screening coming from the inorganic PbI_3^- sublattice. The total energy by summing
 225 over dipole \mathbf{d} at site- m is expressed as:

$$\begin{aligned}
 E_{\text{tot}} &= \sum_m \mathbf{d}_m \cdot \tilde{\mathbf{E}}_m \\
 \tilde{\mathbf{E}}_m &= \frac{1}{\epsilon_n} \sum_n \mathbf{E}_m(n) + \frac{1}{\epsilon_{n'}} \sum_{n'} \mathbf{E}_m(n') + \frac{1}{\epsilon_{n''}} \sum_{n''} \mathbf{E}_m(n'') + \frac{1}{\epsilon_{n'''}} \sum_{n'''} \mathbf{E}_m(n''') \quad (4)
 \end{aligned}$$

226 where $\tilde{\mathbf{E}}_m$ is the screened electric field from other dipoles applied to the dipole at site m .
 227 Here, we believe that dipoles at different distances will have different screening effect from
 228 the PbI_3^- sublattice in order to mimic the reciprocal-vector dependent screening. Therefore,
 229 we partition the spatial summation into four different layers (n : nearest neighbor; n' : next-
 230 nearest neighbor; n'' : third-nearest neighbor; n''' : others) with different dielectric constants.
 231 $\epsilon_{n'''}$ is known as 21, corresponding to the low frequency dielectric constant ϵ_0 . Besides
 232 electric field, the average potential at MA molecule sites ($V_m = \frac{1}{\epsilon_n} \sum_n V_m(n) + \frac{1}{\epsilon_{n'}} \sum_{n'} V_m(n') +$
 233 $\frac{1}{\epsilon_{n''}} \sum_{n''} V_m(n'') + \frac{1}{\epsilon_{n'''}} \sum_{n'''} V_m(n''')$) is screened with the same set of dielectric constants. The
 234 dielectric constants (ϵ_n , $\epsilon_{n'}$, and $\epsilon_{n''}$) are obtained by fitting the *potentials* computed from the
 235 above screened dipole-dipole model to the averaged potentials of a molecule extracted from
 236 DFT calculations (SI) with many random configurations of the MA molecules. For a given
 237 MA orientation configuration, the PbI_3^- sublattice is fully relaxed. Thus, the DFT potential
 238 contains the screening effect of the PbI_3^- sublattice, as described in Eq. 4. Fig. 2 shows the
 239 comparison of the potential obtained between the above model and DFT potential, which
 240 demonstrates the validity of our screening model.

241 After each MC step, their potentials on each Pb and I atoms are re-evaluated. Between
 242 two MC steps, the potential change is interpolated linearly into small time steps ($\sim 0.048\text{fs}$)
 243 in order to carry out the evolution of the wavefunction. The time-dependent wavefunction
 244 evolution are solved following the Schrodinger's equation by applying the evolution operator
 245 to the wavefunction directly:

$$\begin{aligned}
 \psi(t + dt) &= e^{-iH(t)dt} \psi(t) \\
 &\approx \left[1 - iH(t)dt - \frac{1}{2}H^2(t)dt^2 + \frac{i}{6}H^3(t)dt^3 + \frac{1}{24}H^4(t)dt^4 \right] \psi(t) \quad (5)
 \end{aligned}$$

246 The evolution operator is expanded up to the fourth order of dt to ensure the convergence of
 247 the evolution regarding to dt . Here, H is defined in Eq. 2.

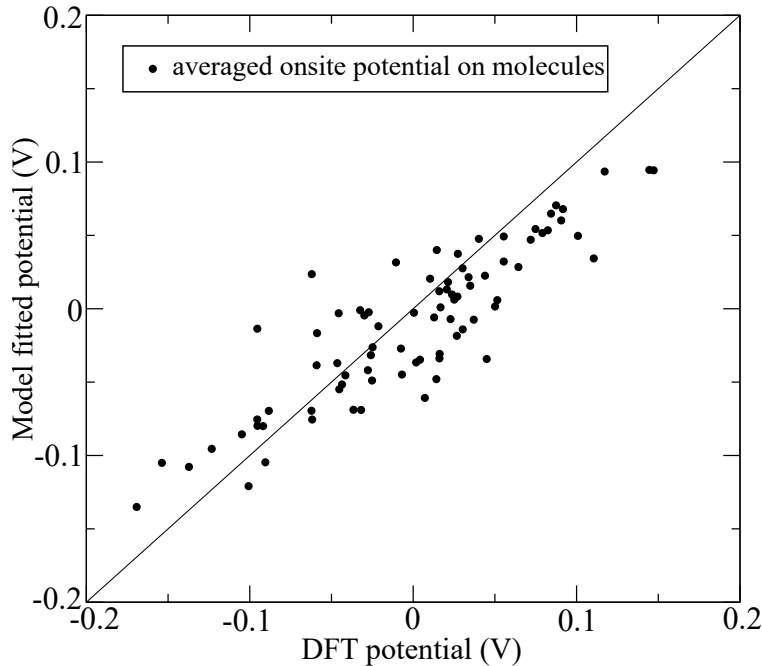


Figure 2: The comparison between the potentials calculated from DFT and the fitted layer-dependent dipole-dipole screening potential.

248 With the setup of Eq. 5, now we can consider the effects of the large polaron. Two effects
 249 are associated with the PbI_3 sublattice. The first is the change of polarization following the
 250 change of charge density $\rho(\mathbf{r})$, the second is the thermal fluctuation of the PbI_3 sublattice.
 251 We first consider the polarization change. The PbI_3 sublattice polarization will follow the
 252 movement of $\rho(\mathbf{r}) = |\psi(\mathbf{r})|^2$. However, such polarization by lattice distortion is not instantane-
 253 ous, instead, some sub-picosecond is needed to form a large polaron as discussed before.
 254 Thus, when the electron hops from one location to a new location, the change of the lattice
 255 screening owing to the new charge density shall also be retarded. To represent this effect,
 256 we mix the old polarization potential and the new potential with a ratio weighted by the
 257 evolution time and the polaron formation time as:

$$V_{t_{n+1}}^{\text{P}} = V_{t_{n+1}}^{\text{Poisson}}[\rho_{t_{n+1}}] \left(1 - e^{-\frac{dt}{\tau}}\right) + V_{t_n}^{\text{P}} e^{-\frac{dt}{\tau}} \quad (6)$$

258 where V^{Poisson} is the instantaneous polarization potential calculated from Poisson solver with

259 charge density $\rho_{t_{n+1}}$, τ is the large polaron formation/annihilation time, and $dt = t_{n+1} - t_n$.
 260 The resulting $V_{t_{n+1}}^P$ is used for the second term in H of Eq. 2. In the experiment, the polaron
 261 formation time has been estimated to be around 0.3 and 0.7 ps for MAPbBr₃ and CsPbBr₃
 262 respectively. There is no estimation of τ for MAPbI₃. In our simulation, we have tested
 263 $\tau = 0$ fs, 80 fs, 150 fs and 300 fs, and large τ only slightly reduce the diffusion constant
 264 (SI). However, the reduction is quite small compared to other factors discussed below. Thus,
 265 we have used $\tau = 80$ fs for our calculations. Such retarded potential is then added to the
 266 Hamiltonian and the wavefunction evolution.

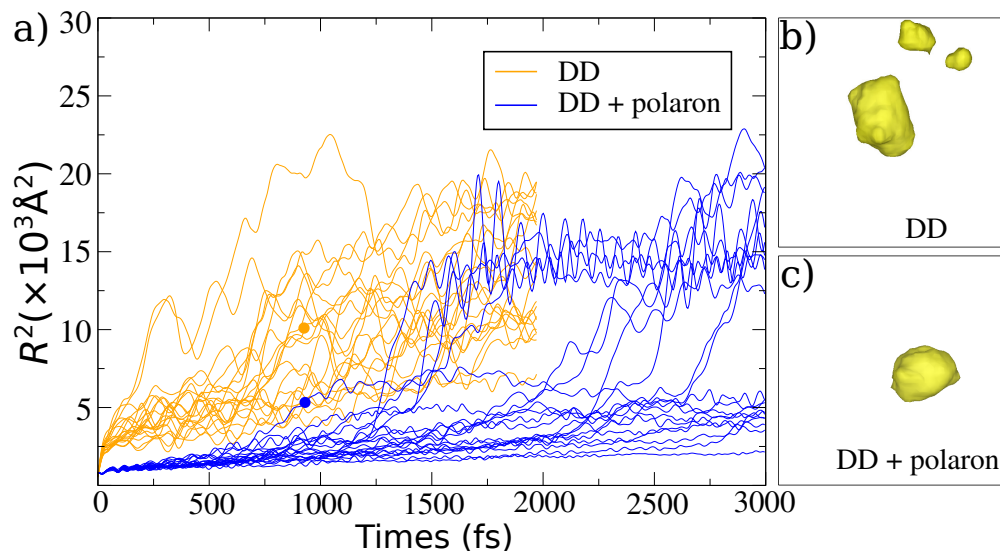


Figure 3: a) $R^2(t)$ of 20 independent trajectories for the case (orange line) with dynamic disorder only (DD) and the case (blue line) with both dynamic disorder and large polaron. The molecular rotation time used in this graph is 6 ps. b) Snapshot of the wavefunction (charge density) for the case with dynamic disorder only at time $t = 900$ fs. This state is picked up from the trajectory with orange dot in a). c) Snapshot of the wavefunction (charge density) for the case with dynamic disorder and large polaron effect at time $t = 900$ fs. This state is picked up from the trajectory with blue dot in a).

267 With this in place, now we can study the effects of polaron on the carrier diffusion. In our
 268 dynamical simulation, the time step dt for the wavefunction evolution is 2 a.u. (around 0.048
 269 fs) to ensure its stability. For every ten dt steps, a MC step is applied to rotate the molecules.
 270 To capture the change of the polaron polarization potential, the Poisson equation is re-solved
 271 based on the charge density for every 5 fs. To quantify the diffusion process, $R^2(t)$ has been

272 calculated as shown by Fig. 3a, where $R^2(t) = \langle \psi(t) | (\mathbf{r} - \mathbf{r}_0)^2 | \psi(t) \rangle$ is evaluated for the
273 localized wavefunctions. \mathbf{r}_0 is the center of mass of the charge density at $t = 0$. The initial
274 wavefunction square $|\psi|^2(t = 0)$ is shown as Fig. 1d. To illustrate the wavefunction evolution,
275 we show the states at $t = 900$ fs for a given trajectory shown in Fig.3a with and without the
276 large polaron effect in Fig. 3b and c, respectively. We can see that the originally localized
277 CBM state in the center of the box starts to diffuse off center in the case with dynamic
278 disorder and large polaron. For the case with dynamic disorder only, the wavefunction has
279 been broken down into a few pieces. In order to further quantify the diffusion of the large
280 polaron, we perform 20 independent trajectories starting from the same initial state with
281 different random MC seeds, with and without the large polaron effect. The $R^2(t)$ of all the
282 20 trajectories are shown in Fig. 3a. For the case without polaron, the carrier can quickly
283 escape from the center after 200 fs from the initial state. Moreover, once the carrier is hopped
284 away, its R^2 value oscillates strongly, indicating a strong spatial variation of the wavefunction
285 in real space. However, by including polaron effect, some of the trajectories have very small
286 increments even after a long time. This corresponds to the situation that these localized
287 states are still in the center and do not get a chance to hop. In general, the carrier needs
288 to spend more than 1ps before it can accumulate enough potential variations in order to
289 overcome the initial polarization potential and hop to a different place. Once the carrier
290 is moved, it tends to stay in a new place for a while before jumping to another location,
291 showing a step-like R^2 . But the important conclusion is that the polarization potential does
292 not completely trap the carrier in a location permanently. The carrier can still move and hop
293 to a new place, albeit such hopping rate is smaller than the case without the large polaron
294 effect. By averaging $R^2(t)$ for all the trajectories, we compute the diffusion coefficient D as
295 $\bar{R}^2(t) = \langle R^2(t) \rangle = 6Dt$.²⁴ The averaged $R^2(t)$ forms a straight line as we expected (Fig. 4a),
296 and the slope of this straight line yields the diffusion constant D . By doing so for each
297 rotation rate, we obtain Fig. 4b, where the diffusion constants are compared for the case
298 with dynamic disorder only and case with dynamic disorder and large polaron polarization

299 (but without yet the thermal fluctuation of the PbI_3^- sublattice). The diffusion constants
 300 without the large polaron effect agree with our previous results in Ref. 24, although some
 301 modifications have been made both for the TB model and the screening model of Eq. 4. The
 302 large polaron reduces the diffusion coefficient by a factor of 2. This is because the additional
 303 polaron polarization potential further localizes wavefunction and deepens the localization
 304 potential, thus makes the hopping more difficult.

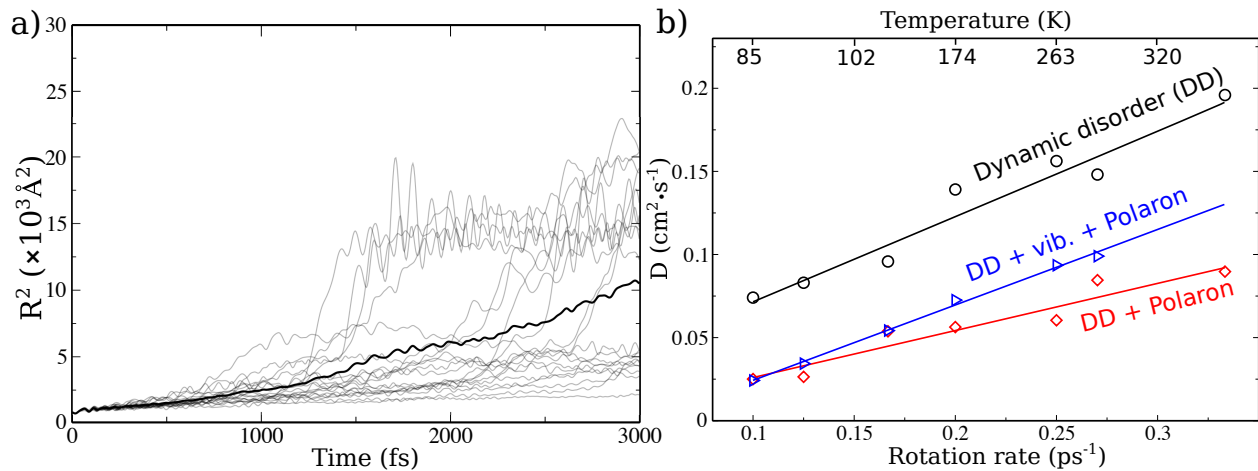


Figure 4: a) The $R^2(t)$ evolution along time for 20 independent trajectories (grey lines) under rotation time at 6 ps. The thick black line indicate the averaged value of the 20 trajectories $\bar{R}^2(t)$. b) The diffusion constant D obtained for different rotation rates for the three cases: dynamic disorder (DD) only, DD + large polaron, DD + PbI_3^- sublattice vibration + large polaron. The temperature T used in the lattice vibration and MC simulation of DD is correlated with the rotation rate as: $\text{rate} \propto e^{-(10\text{meV}/kT)}$.²⁴

305 Up to now, we have discussed the effects of the large polaron and A -site molecular
 306 orientation flipping induced dynamic disorder to the carrier dynamics. Besides forming the
 307 polarization potential in response to the carrier charge density, the thermal vibrations of
 308 PbI_3^- sublattice can also exert a driving force to induce the carrier motion in addition to the
 309 dynamic disorder potential fluctuation. Such thermal vibrational effect can be represented
 310 by the variation of Pb and I onsite potentials and the change of the TB coupling strength
 311 between two neighboring Pb and I atoms. Unfortunately, there is no easy realistic calculation
 312 to capture both effects at the same time. Instead, we have used a model dynamics to describe
 313 the onsite energy fluctuation, and a classical MD to simulate structural distortion which

314 results in the change of TB coupling strength. Note that here, the Pb and I onsite potential
 315 fluctuation refers to the fluctuation caused by the thermal movement of Pb and I atoms, not
 316 the fluctuation caused by the MA molecular rotations, which has been already included in
 317 the dynamic disorder model. This statistic feature of the onsite potential fluctuation can be
 318 collected from a small supercell *ab initio* MD while fixing the MA molecules. Fig. 5 shows the
 319 averaged Pb-, I- onsite auto-correlation function and nearest neighboring Pb–I pair potential
 320 correlation functions, obtained from a DFT trajectory (SI) with fixed MA molecules. The
 321 relatively simple oscillations of the DFT onsite potential auto-correlation functions allow us
 322 to fit it with an onsite Langevin dynamics model comprising of simple oscillators. In this
 323 model dynamics, the equation of motion for one Pb or I is expressed as $\ddot{x} = -c\dot{x} - kx + F_{\text{random}}$,
 324 x is the variable to describe the dynamics of the potential, parameters c and k control
 325 the damping rate and oscillation frequency respectively, and F_{random} is the random force
 326 applied to each Langevin step. These dynamic models are carried out independently for
 327 each atom with different parameters for Pb and I sites, denoting their results as $x_i^{\text{Pb}}(t)$ and
 328 $x_i^{\text{I}}(t)$, and i indicates the lattice site. To yield the correct nearest-neighbor Pb–I correlation
 329 function, we also mix the dynamics of neighboring Pb and I as following: $V_i^{\text{Pb}}(t) = \alpha_1 x_i^{\text{Pb}}(t) +$
 330 $\beta_1 \sum_{\text{neigh}} x_j^{\text{I}}(t)$, $V_i^{\text{I}}(t) = \alpha_2 x_i^{\text{I}}(t) + \beta_2 \sum_{\text{neigh}} x_j^{\text{Pb}}(t)$, here $V_i^{\text{Pb}}(t)$ and $V_i^{\text{I}}(t)$ are the final Pb and
 331 I onsite potential to be added in H_0 with α and β as fitting parameters. All the parameters
 332 used in the model and the mixing weights are tuned so that both the onsite auto-correlation
 333 function and neighboring-pair correlation functions of $V_i^{\text{Pb}}(t)$ and $V_i^{\text{I}}(t)$ match DFT as
 334 shown in Fig. 5. Using this model dynamics, the full onsite potential time evolution profiles
 335 of all the Pb and I atoms in the $48 \times 48 \times 48$ supercell can be obtained. Meanwhile, in order
 336 to simulate the PbI_3^- sublattice vibration thus its effects on TB coupling, we performed
 337 the classical MD with LAMMPS⁶⁸ using force field designed for MAPbI_3 for the $48 \times 48 \times 48$
 338 supercell at different temperatures⁶⁹ (SI). Our tight-binding model is capable to evaluate
 339 the change of the hopping strength based on the Pb–I bond-length deviation with the general
 340 form $h = h_0 e^{-\lambda(b-b_0)}$, where h_0 and b_0 are the equilibrium hopping strength and bond length,

341 respectively. Here, λ of different bond types are given from Ref. 70, where they are fitted
 342 by the Wannierization of large number of structures with different bond distortions.

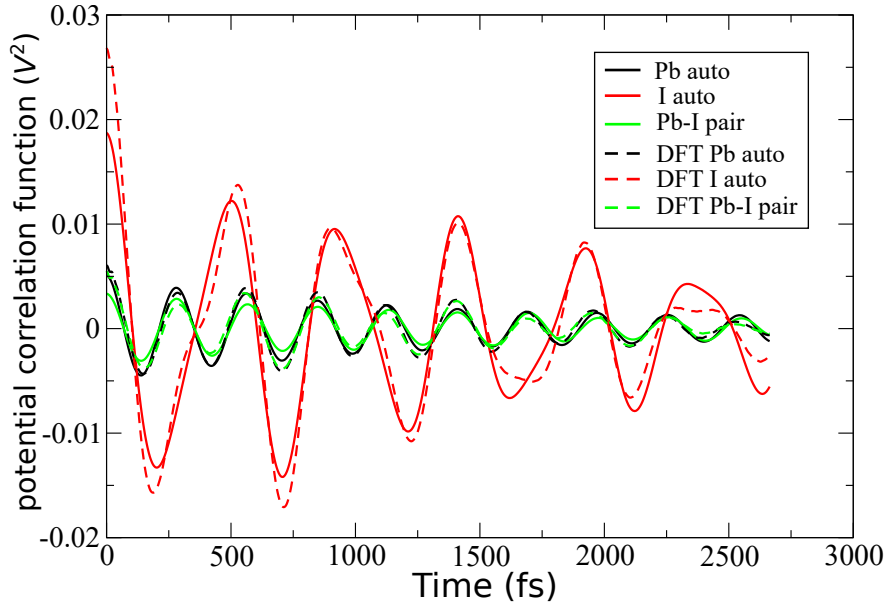


Figure 5: a) The Pb autocorrelation, I autocorrelation, neighboring Pb–I pair correlation functions computed from Langevin model dynamics and DFT *ab initio* MD.

343 With the onsite potential and the local TB coupling parameter time evolution profiles
 344 for the $48 \times 48 \times 48$ supercell, the PbI_3 sublattice thermal vibration effect is added to the
 345 time-evolution of the wavefunctions described by Eq. 5. All these effects are included in
 346 H_0 of Eq. 2. Owing to the relatively slow change of the onsite potential and bond length
 347 by phonons, we update the PbI_3 structure and the corresponding parameters for every 5
 348 fs. During the 5 fs, the onsite energies and the hoppings are interpolated linearly to small
 349 dt to evolve the wavefunction. To investigate the sublattice vibrational effects at different
 350 temperatures, we have calculated the diffusion constants at different temperatures including
 351 the effects of dynamic disorder, large polaron and sublattice vibration as shown in Fig. 4.
 352 In Fig. 4, we have used the MA molecular rotation rate as the horizontal axis while using a
 353 rate $\gamma \propto e^{-E_a/kT}$ by assuming the MA rotation activation energy $E_a = 10$ meV to correlate
 354 between different MA rotation rate and temperature T .²⁴ Intuitively, the sublattice vibration
 355 should enhance the carrier diffusion for all the temperatures, because the onsite potential

356 variation and TB coupling strength change tend to offer additional random driving force for
357 the carrier movement in addition to the dynamic disorder caused by molecular re-orientation.
358 However, our simulation shows such effect is not homogeneous at different rotation rates. At
359 high rotation rate (also high temperature), the enhancement of carrier mobility is obvious.
360 While, at the low rotation rate (low temperature), the increase is less pronounced. We think
361 this is because there are actually two possible effects of the PbI_3^- sublattice vibration, similar
362 to the that of the MA molecule re-orientation. The fluctuation caused by PbI_3^- sublattice
363 vibration can also further localize the carrier, in addition to providing the movement driving
364 force. Such enhanced localization introduces deeper polaron polarization potential, and
365 tend to slow down the carrier motion. This is illustrated in Fig. S6, where the lowest
366 polaron potentials are extracted. By rotating exactly same molecular dipoles every MC
367 step for the two cases with and without PbI_3^- sublattice vibrational effect, the polarization
368 potential difference is purely caused by the sublattice vibrations, and such effect deepens
369 the polarization potential. It seems that the two effects of PbI_3^- vibration are competing
370 with each other. Perhaps at higher temperature, the driving force effect dominates, hence it
371 increases the carrier diffusion, while in lower temperature, there two effects cancel out each
372 other.

373 After the diffusion constant is obtained, the mobility can be evaluated by $\mu = D/k_{\text{B}}T$.
374 However, the carrier mobilities vary widely from different experiments³⁰ (Fig.6). Even for the
375 mobilities measured with the same method, their values could be quite different. Therefore,
376 it is very difficult to compare with the experiments directly. Our calculated mobility is
377 found to be close to the experimental value. By adding the polaron effect, the mobility of
378 the carriers is reduced by half. However, the effect of the PbI_3^- sublattice vibration tends
379 to shift up the mobility, into the range of 3 to 5 $\text{cm}^2\text{V}^{-1}\text{s}^{-1}$ at the molecular rotation rate
380 between 3ps to 10ps. Overall, our results agree with the experiments as we have shown
381 for comparison,^{71,72} especially for the trend. If we fit the temperature-mobility dependence
382 to the relation $\mu \propto T^k$ for full temperature range, $k=-0.523$ (DD), -0.448 (DD+Polaron),

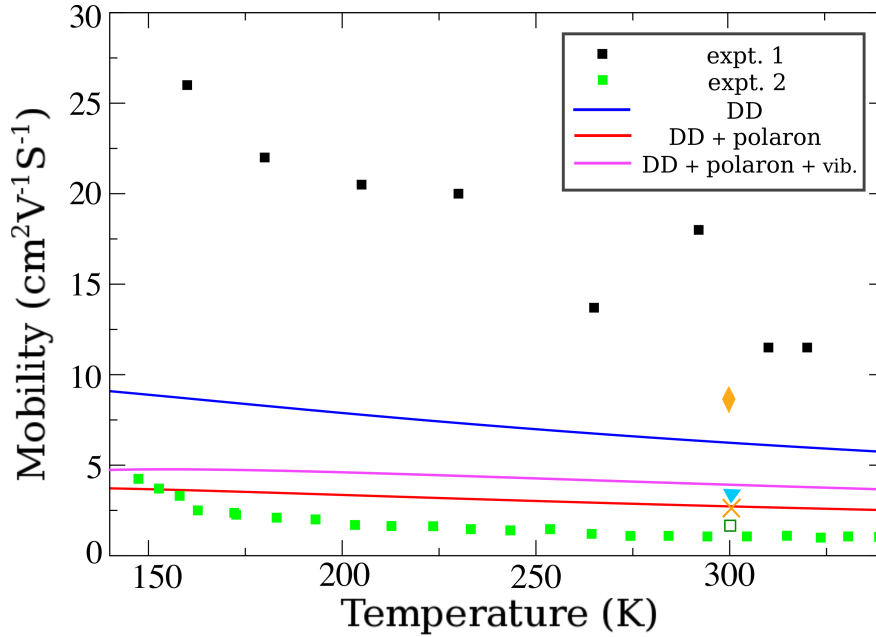


Figure 6: The calculated mobility with respect to the temperature considering different effects: dynamic disorder (DD) only, DD+large polaron, DD+large polaron+ PbI_3 phonon. The experimental values are from Ref. 71 for expt. 1 and Ref. 72 for expt. 2. Other experimental measured mobilities are also listed, \times : Ref. 73 (μ_e), \blacktriangledown : Ref. 74 (μ_e), \square : Ref. 75 ($\mu_e + \mu_h$), \blacklozenge : Ref. 76 ($\mu_e + \mu_h$).

383 and -0.318 (DD+Polaron+vib) are obtained. Similar to the measured mobilities, values of k
384 could be quite different. Many experiments have yielded $k \approx -1.5$ ^{71,72,77,78} fitted for tetragonal
385 phase only or together with orthogonal phases, but other values $k = -2.8(e^-)$ and $-2.0(h^+)$ are
386 also obtained.⁷⁹ However, the dynamic disorder effect caused by the molecules becomes more
387 prominent at high temperature. At low temperature, the rotation of the molecules is further
388 constrained by the PbI_3 sublattice, and their orientation becomes more ordered,⁸⁰ which may
389 suppress the carrier localization. Meanwhile, ϵ_0 could have strong temperature dependence
390 at low temperature, which alters polaron polarization screening. Therefore, if we fit k only in
391 high temperature range (for example $>290\text{K}$), we obtain $k = -0.65$ (DD), -0.63 (DD+Polaron),
392 and -0.55 (DD+Polaron+vib). This result is in line with $k = -0.42$, fitted from the measured
393 mobilities of experiment 2⁷² at high temperature range ($>290\text{K}$). Recent theoretical work⁶²
394 also achieve k value around -0.46 , consistent to what we get. Considering the differences
395 of experiment 1 and 2, in experiment 1,⁷¹ they used PL and THz conductivity spectra to

396 study the temperature dependent mobility. In experiment 2,⁷² the time-resolved microwave
397 conductivity technique was used to explore effect of *A*-site cation to the carrier dynamics.
398 The reason for the large difference between the two experiments could be complicated, it
399 might depend on the sample condition due to different synthesise conditions etc. If we
400 assume the sample conditions are the same, then the better agreement with experiment 2
401 could be because the electric field used in microwave probe is weak,⁷² which is consistent
402 with the weak field limit in our calculation. The strong electric field in THz measurement
403 may introduce non-linear mobility effect, as the potential drop caused by each hopping is in
404 the same order as the potential barrier for the wavefunction localization. Furthermore, the
405 THz frequency time is similar to the phonon frequency, which in some degree might freeze
406 the lattice polarization in its measurement. As a result, its measured mobility might be
407 more close to our previous study without large polaron effects, as shown in Fig.6. In our
408 current simulation, the *A*-site is occupied by the polar molecules. For pure inorganic halide
409 perovskite such as CsPbX₃, the displacement of Cs⁺ atom will contribute to the formation
410 of the large polarons. However, without the slow rotational degree of freedom of the *A*-site
411 molecule, the large polaron may be hard to form, and it will have a much smaller binding
412 energy. This may explain the higher mobility observed in CsPbBr₃.^{26,72,81} In this work, the
413 large polaron of the hole is not discussed. However, as shown in our previous work,²³ the
414 electron and hole are localized at different locations due to the potential fluctuation caused
415 by the random orientation of the MA molecule. Large polaron tends to further localize them,
416 thus their reduced spatial overlap may lower the radiative recombination and enhance the
417 lifetime.

418 In the end, we want to justify the hopping picture and the BO approximation we have used
419 throughout this work. There have been continuous efforts to understand the large polaron
420 in hybrid perovskites, e.g. using Bloch state as the starting point to include the scattering of
421 optical phonon modes.³¹ For a conventional perfect crystal structure such as GaAs with weak
422 electron-phonon coupling, the Boltzmann equation is more appropriate to describe the large

423 polaron transport with the Bloch state as a starting point,⁸² although there are also attempts
424 to use hopping picture for large polaron transport even in perfect crystal,⁸³ However, hybrid
425 perovskite including MAPbI₃ is not a usual “perfect crystal”. Recent experiments and
426 theoretical work have shown the strong electron-phonon coupling and indicated that the
427 carrier could be localized under the random orientation of *A*-site molecules, which is also
428 why these materials are unusual and fascinating. Under this circumstance, the charge is
429 already localized before any additional large polaron induced localization. Thus, the hopping
430 picture of such localized charge is more appropriate to study its transport. This is different
431 from the hopping picture used for small polarons, where the localized states hops between
432 nearby bonds within a unit cell. In this work, the hopping distance is typically comparable
433 to the localization size, thus much larger than the nearest neighbor atomic distance. As for
434 the BO approximation, when electron-phonon coupling is small (weak-coupling limit, such
435 as GaAs), the phonon affects the electronic structure in a perturbed way. The electron and
436 phonon are correlated dynamically, and the BO approximation is unsuitable. However, when
437 electron-phonon interaction is strong (strong-coupling limit), the phonon cannot respond to
438 the fast electron movement to necessitate the correlated perturbation treatment. Therefore,
439 the adiabatic BO approximation can be used, as discussed in this work. Another important
440 reason for the BO approximation is that, as discussed above, the wavefunction is already
441 localized under dynamic disorder before any polaron effect, which will significantly reduce
442 the correlation effect. As we show in our paper, the polaron binding energy for a localized
443 electron becomes much larger. Under our adiabatic approximation, these two localizations
444 (caused by large polaron and dynamic disorder) are treated on equal footing, there is no
445 approximation between them (not treating one as an perturbation to another). Of course,
446 the perfect method to solve the large polaron at any coupling is to use Feynman’s path
447 integral. But this is still hard to apply to a realistic system at the atomic level.

448 *Summary.* In summary, by using the tight-binding model fitted to the first-principles
449 DFT calculations, we studied the large polaron formation and its effects on carrier transport

450 in MAPbI₃. We provide an atomic and quantitative picture to understand the large polaron
451 effect in MAPbI₃. We studied two effects of the PbI₃⁻ sublattice to the carrier mobility.
452 The first is the large polaron polarization effect, which tends to further localize the carrier
453 wavefunction on top of the dynamic disorder caused by MA molecule rotation. The second
454 is the thermal vibration of the PbI₃⁻ sublattice which provides randomness to further localize
455 the wavefunction, but also a driving force for carrier movement. Our calculation shows a
456 large polaron with formation energy around 12 meV for one electron carrier when there
457 is no molecular disorder, which is consistent with the Fröhlich model at strong coupling
458 limit. By adding dynamic disorder, the large polaron binding energy is increased to 55 meV.
459 This polaron state is accomplished by a lattice polarization potential around 0.14 eV, only
460 slightly smaller than the 0.2 eV potential fluctuation caused by the MA molecular random
461 orientation. By solving the time-dependent Schrodinger's equation and performing MC
462 simulation, we study how the electron state evolves under the driving force of the molecular
463 re-orientation and the lattice vibration. We find that the polaron effect slows down the
464 mobility of the electrons by a factor of 2. On the other hand, the PbI₃⁻ sublattice vibration
465 enhances the electron mobility particularly at high temperature. Overall, the computed
466 mobility is in line with the experimental measurements. Our calculation reveals how the
467 large polaron state is formed and its role in carrier movement in the MAPbI₃ system.

468 **Acknowledgement**

469 This material is based on the work performed by the Joint Center for Artificial Photosyn-
470 thesis, a DOE Energy Innovation Hub, supported through the Office of Science of the U.S.
471 Department of Energy under Award number DE-SC0004993. We use the resource of Na-
472 tional Energy Research Scientific Computing center (NERSC) located in Lawrence Berkeley
473 National Laboratory. We thank Liang Z. Tan, Shi Liu, and Andrew Rappe for the discus-
474 sions and their help to the TB model used in this work. We thank Alessandro Mattoni for

475 the discussions and his help to the classical MD simulation.

476 References

- 477 (1) Buin, A.; Pietsch, P.; Xu, J.; Voznyy, O.; Ip, A. H.; Comin, R.; Sargent, E. H. Materials
478 Processing Routes to Trap-Free Halide Perovskites. *Nano Letters* **2014**, *14*, 6281–6286.
- 479 (2) Kim, J.; Lee, S.-H.; Lee, J. H.; Hong, K.-H. The Role of Intrinsic Defects in Methylam-
480 monium Lead Iodide Perovskite. *The Journal of Physical Chemistry Letters* **2014**, *5*,
481 1312–1317.
- 482 (3) Kang, J.; Wang, L.-W. High Defect Tolerance in Lead Halide Perovskite CsPbBr₃. *The*
483 *Journal of Physical Chemistry Letters* **2017**, *8*, 489–493.
- 484 (4) Yin, W.-J.; Shi, T.; Yan, Y. Unusual Defect Physics in CH₃NH₃PbI₃ Perovskite Solar
485 Cell Absorber. *Applied Physics Letters* **2014**, *104*, 063903.
- 486 (5) Brenner, T. M.; Egger, D. A.; Kronik, L.; Hodes, G.; Cahen, D. Hybrid Or-
487 ganic–inorganic Perovskites: Low-Cost Semiconductors with Intriguing Charge-
488 Transport Properties. *Nature Reviews Materials* **2016**, *1*, 15007.
- 489 (6) Stranks, S. D.; Eperon, G. E.; Grancini, G.; Menelaou, C.; Alcocer, M. J. P.; Lei-
490 jtens, T.; Herz, L. M.; Petrozza, A.; Snaith, H. J. Electron-Hole Diffusion Lengths
491 Exceeding 1 Micrometer in an Organometal Trihalide Perovskite Absorber. *Science*
492 **2013**, *342*, 341–344.
- 493 (7) Zhu, H.; Miyata, K.; Fu, Y.; Wang, J.; Joshi, P. P.; Niesner, D.; Williams, K. W.;
494 Jin, S.; Zhu, X.-Y. Screening in Crystalline Liquids Protects Energetic Carriers in
495 Hybrid Perovskites. *Science* **2016**, *353*, 1409–1413.
- 496 (8) Dong, Q.; Fang, Y.; Shao, Y.; Mulligan, P.; Qiu, J.; Cao, L.; Huang, J. Electron-

- 497 Hole Diffusion Lengths > 175 *Mm* in Solution-Grown CH₃NH₃PbI₃ Single Crystals.
498 *Science* **2015**, *347*, 967–970.
- 499 (9) Brenner, T. M.; Egger, D. A.; Rappe, A. M.; Kronik, L.; Hodes, G.; Cahen, D. Are Mo-
500 bilities in Hybrid Organic–Inorganic Halide Perovskites Actually “High”? *The Journal*
501 *of Physical Chemistry Letters* **2015**, *6*, 4754–4757.
- 502 (10) Frost, J. M.; Butler, K. T.; Brivio, F.; Hendon, C. H.; van Schilfgaarde, M.; Walsh, A.
503 Atomistic Origins of High-Performance in Hybrid Halide Perovskite Solar Cells. *Nano*
504 *Letters* **2014**, *14*, 2584–2590.
- 505 (11) Liu, S.; Zheng, F.; Koocher, N. Z.; Takenaka, H.; Wang, F.; Rappe, A. M. Ferroelectric
506 Domain Wall Induced Band Gap Reduction and Charge Separation in Organometal
507 Halide Perovskites. *The Journal of Physical Chemistry Letters* **2015**, *6*, 693–699.
- 508 (12) Rashkeev, S. N.; El-Mellouhi, F.; Kais, S.; Alharbi, F. H. Domain Walls Conductivity
509 in Hybrid Organometallic Perovskites and Their Essential Role in CH₃NH₃PbI₃ Solar
510 Cell High Performance. *Scientific Reports* **2015**, *5*, 11467.
- 511 (13) Chen, Y.-F.; Tsai, Y.-T.; Bassani, D. M.; Hirsch, L. Experimental Evidence of the
512 Anti-Parallel Arrangement of Methylammonium Ions in Perovskites. *Applied Physics*
513 *Letters* **2016**, *109*, 213504.
- 514 (14) Frost, J. M.; Butler, K. T.; Walsh, A. Molecular Ferroelectric Contributions to Anoma-
515 lous Hysteresis in Hybrid Perovskite Solar Cells. *APL MATERIALS* **2014**, *2*, 081506.
- 516 (15) Zheng, F.; Tan, L. Z.; Liu, S.; Rappe, A. M. Rashba Spin–Orbit Coupling Enhanced
517 Carrier Lifetime in CH₃NH₃PbI₃. *Nano Letters* **2015**, *15*, 7794–7800.
- 518 (16) Even, J.; Pedesseau, L.; Katan, C. Comment on “Density Functional Theory Analysis
519 of Structural and Electronic Properties of Orthorhombic Perovskite CH₃NH₃PbI₃

- 520 ” by Y. Wang et Al., *Phys. Chem. Chem. Phys.*, 2014, **16** , 1424–1429. *Phys. Chem.*
521 *Chem. Phys.* **2014**, *16*, 8697–8698.
- 522 (17) Motta, C.; El-Mellouhi, F.; Kais, S.; Tabet, N.; Alharbi, F.; Sanvito, S. Revealing the
523 Role of Organic Cations in Hybrid Halide Perovskite CH₃NH₃PbI₃. *Nature Communi-*
524 *cations* **2015**, *6*, 7026.
- 525 (18) Etienne, T.; Mosconi, E.; De Angelis, F. Dynamical Origin of the Rashba Effect in
526 Organohalide Lead Perovskites: A Key to Suppressed Carrier Recombination in Per-
527 ovskite Solar Cells? *The Journal of Physical Chemistry Letters* **2016**, *7*, 1638–1645.
- 528 (19) Rakita, Y.; Bar-Elli, O.; Meirzadeh, E.; Kaslasi, H.; Peleg, Y.; Hodes, G.;
529 Lubomirsky, I.; Oron, D.; Ehre, D.; Cahen, D. Tetragonal CH₃NH₃PbI₃ Is Ferro-
530 electric. *Proceedings of the National Academy of Sciences* **2017**, *114*, E5504–E5512.
- 531 (20) Fan, Z.; Xiao, J.; Sun, K.; Chen, L.; Hu, Y.; Ouyang, J.; Ong, K. P.; Zeng, K.; Wang, J.
532 Ferroelectricity of CH₃NH₃PbI₃ Perovskite. *The Journal of Physical Chemistry*
533 *Letters* **2015**, *6*, 1155–1161.
- 534 (21) Dastidar, S.; Li, S.; Smolin, S. Y.; Baxter, J. B.; Fafarman, A. T. Slow Electron–Hole
535 Recombination in Lead Iodide Perovskites Does Not Require a Molecular Dipole. *ACS*
536 *Energy Letters* **2017**, *2*, 2239–2244.
- 537 (22) Yaffe, O.; Guo, Y.; Tan, L. Z.; Egger, D. A.; Hull, T.; Stoumpos, C. C.; Zheng, F.;
538 Heinz, T. F.; Kronik, L.; Kanatzidis, M. G.; Owen, J. S.; Rappe, A. M.; Pimenta, M. A.;
539 Brus, L. E. Local Polar Fluctuations in Lead Halide Perovskite Crystals. *Physical Re-*
540 *view Letters* **2017**, *118*, 136001.
- 541 (23) Ma, J.; Wang, L.-W. Nanoscale Charge Localization Induced by Random Orientations
542 of Organic Molecules in Hybrid Perovskite CH₃NH₃PbI₃. *Nano Letters* **2015**, *15*,
543 248–253.

- 544 (24) Ma, J.; Wang, L.-W. The Nature of Electron Mobility in Hybrid Perovskite $\text{CH}_3\text{NH}_3\text{PbI}_3$. *Nano Letters* **2017**, *17*, 3646–3654.
545
- 546 (25) Ambrosio, F.; Wiktor, J.; Angelis, F. D.; Pasquarello, A. Origin of Low Electron–hole
547 Recombination Rate in Metal Halide Perovskites. *Energy & Environmental Science*
548 **2018**, *11*, 101–105.
- 549 (26) Kang, J.; Wang, L.-W. Dynamic Disorder and Potential Fluctuation in Two-
550 Dimensional Perovskite. *The Journal of Physical Chemistry Letters* **2017**, *8*, 3875–
551 3880.
- 552 (27) Frost, J. M.; Whalley, L. D.; Walsh, A. Slow Cooling of Hot Polarons in Halide Per-
553 ovskite Solar Cells. *ACS Energy Letters* **2017**, *2*, 2647–2652.
- 554 (28) Kawai, H.; Giorgi, G.; Marini, A.; Yamashita, K. The Mechanism of Slow Hot-Hole
555 Cooling in Lead-Iodide Perovskite: First-Principles Calculation on Carrier Lifetime
556 from Electron–Phonon Interaction. *Nano Letters* **2015**, *15*, 3103–3108.
- 557 (29) Wright, A. D.; Verdi, C.; Milot, R. L.; Eperon, G. E.; Pérez-Osorio, M. A.; Snaith, H. J.;
558 Giustino, F.; Johnston, M. B.; Herz, L. M. Electron–phonon Coupling in Hybrid Lead
559 Halide Perovskites. *Nature Communications* **2016**, *7*, 11755.
- 560 (30) Herz, L. M. Charge-Carrier Mobilities in Metal Halide Perovskites: Fundamental Mech-
561 anisms and Limits. *ACS Energy Letters* **2017**, *2*, 1539–1548.
- 562 (31) Yu, Z.-G. Rashba Effect and Carrier Mobility in Hybrid Organic–Inorganic Perovskites.
563 *The Journal of Physical Chemistry Letters* **2016**, *7*, 3078–3083.
- 564 (32) Zhu, X.-Y.; Podzorov, V. Charge Carriers in Hybrid Organic–Inorganic Lead Halide
565 Perovskites Might Be Protected as Large Polarons. *The Journal of Physical Chemistry*
566 *Letters* **2015**, *6*, 4758–4761.

- 567 (33) Bischak, C. G.; Hetherington, C. L.; Wu, H.; Aloni, S.; Ogletree, D. F.; Limmer, D. T.;
568 Ginsberg, N. S. Origin of Reversible Photoinduced Phase Separation in Hybrid Per-
569 ovskites. *Nano Letters* **2017**, *17*, 1028–1033.
- 570 (34) Ivanovska, T.; Dionigi, C.; Mosconi, E.; De Angelis, F.; Liscio, F.; Morandi, V.; Ru-
571 ani, G. Long-Lived Photoinduced Polarons in Organohalide Perovskites. *The Journal*
572 *of Physical Chemistry Letters* **2017**, *8*, 3081–3086.
- 573 (35) Neukirch, A. J.; Nie, W.; Blancon, J.-C.; Appavoo, K.; Tsai, H.; Sfeir, M. Y.; Katan, C.;
574 Pedesseau, L.; Even, J.; Crochet, J. J.; Gupta, G.; Mohite, A. D.; Tretiak, S. Polaron
575 Stabilization by Cooperative Lattice Distortion and Cation Rotations in Hybrid Per-
576 ovskite Materials. *Nano Letters* **2016**, *16*, 3809–3816.
- 577 (36) Welch, E.; Scolfaro, L.; Zakhidov, A. Density Functional Theory + U Modeling of
578 Polarons in Organohalide Lead Perovskites. *AIP Advances* **2016**, *6*, 125037.
- 579 (37) Nie, W.; Blancon, J.-C.; Neukirch, A. J.; Appavoo, K.; Tsai, H.; Chhowalla, M.;
580 Alam, M. A.; Sfeir, M. Y.; Katan, C.; Even, J.; Tretiak, S.; Crochet, J. J.; Gupta, G.;
581 Mohite, A. D. Light-Activated Photocurrent Degradation and Self-Healing in Perovskite
582 Solar Cells. *Nature Communications* **2016**, *7*, 11574.
- 583 (38) FzvnMAN, R. P.; Institute, C. Slow Electrons in a Polar Crystal. 6.
- 584 (39) Niesner, D.; Zhu, H.; Miyata, K.; Joshi, P. P.; Evans, T. J. S.; Kudisch, B. J.;
585 Trinh, M. T.; Marks, M.; Zhu, X.-Y. Persistent Energetic Electrons in Methylammo-
586 nium Lead Iodide Perovskite Thin Films. *Journal of the American Chemical Society*
587 **2016**, *138*, 15717–15726.
- 588 (40) Guo, Z.; Wan, Y.; Yang, M.; Snaider, J.; Zhu, K.; Huang, L. Long-Range Hot-Carrier
589 Transport in Hybrid Perovskites Visualized by Ultrafast Microscopy. *Science* **2017**,
590 *356*, 59–62.

- 591 (41) Price, M. B.; Butkus, J.; Jellicoe, T. C.; Sadhanala, A.; Briane, A.; Halpert, J. E.;
592 Broch, K.; Hodgkiss, J. M.; Friend, R. H.; Deschler, F. Hot-Carrier Cooling and Pho-
593 toinduced Refractive Index Changes in Organic–inorganic Lead Halide Perovskites.
594 *Nature Communications* **2015**, *6*, 8420.
- 595 (42) Zhu, Z.; Ma, J.; Wang, Z.; Mu, C.; Fan, Z.; Du, L.; Bai, Y.; Fan, L.; Yan, H.;
596 Phillips, D. L.; Yang, S. Efficiency Enhancement of Perovskite Solar Cells through Fast
597 Electron Extraction: The Role of Graphene Quantum Dots. *Journal of the American*
598 *Chemical Society* **2014**, *136*, 3760–3763.
- 599 (43) Yang, J. et al. Acoustic-Optical Phonon up-Conversion and Hot-Phonon Bottleneck in
600 Lead-Halide Perovskites. *Nature Communications* **2017**, *8*, 14120.
- 601 (44) Yang, Y.; Ostrowski, D. P.; France, R. M.; Zhu, K.; van de Lagemaat, J.; Luther, J. M.;
602 Beard, M. C. Observation of a Hot-Phonon Bottleneck in Lead-Iodide Perovskites.
603 *Nature Photonics* **2016**, *10*, 53–59.
- 604 (45) Miyata, K.; Atallah, T. L.; Zhu, X.-Y. Lead Halide Perovskites: Crystal-Liquid Duality,
605 Phonon Glass Electron Crystals, and Large Polaron Formation. *Science Advances* **2017**,
606 *3*, e1701469.
- 607 (46) Miyata, K.; Meggiolaro, D.; Trinh, M. T.; Joshi, P. P.; Mosconi, E.; Jones, S. C.;
608 Angelis, F. D.; Zhu, X.-Y. Large Polarons in Lead Halide Perovskites. *Science Advances*
609 **2017**, *3*, e1701217.
- 610 (47) Fröhlich, H. Electrons in Lattice Fields. *Advances in Physics* **1954**, *3*, 325–361.
- 611 (48) Jia, W.; Cao, Z.; Wang, L.; Fu, J.; Chi, X.; Gao, W.; Wang, L.-W. The Analysis of
612 a Plane Wave Pseudopotential Density Functional Theory Code on a GPU Machine.
613 *Computer Physics Communications* **2013**, *184*, 9–18.

- 614 (49) Jia, W.; Fu, J.; Cao, Z.; Wang, L.; Chi, X.; Gao, W.; Wang, L.-W. Fast Plane Wave
615 Density Functional Theory Molecular Dynamics Calculations on Multi-GPU Machines.
616 *Journal of Computational Physics* **2013**, *251*, 102–115.
- 617 (50) Perdew, J. P.; Burke, K.; Ernzerhof, M. Generalized Gradient Approximation Made
618 Simple. *Physical review letters* **1996**, *77*, 3865.
- 619 (51) Zheng, F.; Brehm, J. A.; Young, S. M.; Kim, Y.; Rappe, A. M. Substantial Optical
620 Dielectric Enhancement by Volume Compression in LiAsSe 2. *Physical Review B* **2016**,
621 *93*.
- 622 (52) Hamann, D. R. Optimized Norm-Conserving Vanderbilt Pseudopotentials. *Physical Re-*
623 *view B* **2013**, *88*, 085117.
- 624 (53) Giannozzi, P. et al. QUANTUM ESPRESSO: A Modular and Open-Source Software
625 Project for Quantum Simulations of Materials. *Journal of Physics: Condensed Matter*
626 **2009**, *21*, 395502.
- 627 (54) Marzari, N.; Mostofi, A. A.; Yates, J. R.; Souza, I.; Vanderbilt, D. Maximally Localized
628 Wannier Functions: Theory and Applications. *Reviews of Modern Physics* **2012**, *84*,
629 1419–1475.
- 630 (55) Zheng, F.; Takenaka, H.; Wang, F.; Koocher, N. Z.; Rappe, A. M. First-Principles
631 Calculation of the Bulk Photovoltaic Effect in $\text{CH}_3\text{NH}_3\text{PbI}_3$ and $\text{CH}_3\text{NH}_3\text{PbI}_{3-x}\text{Cl}_x$. *The Journal of Physical Chemistry Letters* **2015**, *6*, 31–37.
- 633 (56) Amat, A.; Mosconi, E.; Ronca, E.; Quarti, C.; Umari, P.; Nazeeruddin, M. K.;
634 Grätzel, M.; De Angelis, F. Cation-Induced Band-Gap Tuning in Organohalide Per-
635 ovskites: Interplay of Spin–Orbit Coupling and Octahedra Tilting. *Nano Letters* **2014**,
636 *14*, 3608–3616.

- 637 (57) Kim, M.; Im, J.; Freeman, A. J.; Ihm, J.; Jin, H. Switchable $S = 1/2$ and $J = 1/2$
638 Rashba Bands in Ferroelectric Halide Perovskites. *Proceedings of the National Academy*
639 *of Sciences* **2014**, *111*, 6900–6904.
- 640 (58) Maschho, K. J.; Sorensen, D. C. P ARPACK: An Efficient Portable Large Scale Eigen-
641 value Package for Distributed Memory Parallel Architectures. *Applied Parallel Com-*
642 *puting in Industrial Problems and Optimization, Lecture Notes in Computer Science*
643 **1996**, *1184*.
- 644 (59) Yaffe, O.; Guo, Y.; Tan, L. Z.; Egger, D. A.; Hull, T.; Stoumpos, C. C.; Zheng, F.;
645 Heinz, T. F.; Kronik, L.; Kanatzidis, M. G.; Owen, J. S.; Rappe, A. M.; Pimenta, M. A.;
646 Brus, L. E. Local Polar Fluctuations in Lead Halide Perovskite Crystals. *Physical Re-*
647 *view Letters* **2017**, *118*, 136001.
- 648 (60) Sendner, M.; K. Nayak, P.; A. Egger, D.; Beck, S.; Müller, C.; Epping, B.; Kowal-
649 sky, W.; Kronik, L.; J. Snaith, H.; Pucci, A.; Lovrinčić, R. Optical Phonons in Methy-
650 lammonium Lead Halide Perovskites and Implications for Charge Transport. *Materials*
651 *Horizons* **2016**, *3*, 613–620.
- 652 (61) Kirchartz, T.; Markvart, T.; Rau, U.; Egger, D. A. Impact of Small Phonon Energies on
653 the Charge-Carrier Lifetimes in Metal-Halide Perovskites. *arXiv:1801.02169 [cond-mat]*
654 **2018**,
- 655 (62) Frost, J. M. Calculating Polaron Mobility in Halide Perovskites. *Physical Review B*
656 **2017**, *96*.
- 657 (63) Pérez-Osorio, M. A.; Milot, R. L.; Filip, M. R.; Patel, J. B.; Herz, L. M.; John-
658 ston, M. B.; Giustino, F. Vibrational Properties of the Organic–Inorganic Halide Per-
659 ovskite $\text{CH}_3\text{NH}_3\text{PbI}_3$ from Theory and Experiment: Factor Group Analysis, First-
660 Principles Calculations, and Low-Temperature Infrared Spectra. *The Journal of Phys-*
661 *ical Chemistry C* **2015**, *119*, 25703–25718.

- 662 (64) Muljarov, E. A.; Zimmermann, R. Exciton Dephasing in Quantum Dots Due to LO-
663 Phonon Coupling: An Exactly Solvable Model. *Physical Review Letters* **2007**, *98*.
- 664 (65) Verbist, G.; Peeters, F. M.; Devreese, J. T. Extended Stability Region for Large Bipolarons through Interaction with Multiple Phonon Branches. *Ferroelectrics* **1992**, *130*,
665 27–34.
666
- 667 (66) Zheng, K.; Abdellah, M.; Zhu, Q.; Kong, Q.; Jennings, G.; Kurtz, C. A.; Messing, M. E.;
668 Niu, Y.; Gosztola, D. J.; Al-Marri, M. J.; Zhang, X.; Pullerits, T.; Canton, S. E. Direct
669 Experimental Evidence for Photoinduced Strong-Coupling Polarons in Organolead
670 Halide Perovskite Nanoparticles. *The Journal of Physical Chemistry Letters* **2016**, *7*,
671 4535–4539.
- 672 (67) Devreese, J. T. Frohlich Polarons. Lecture Course Including Detailed Theoretical
673 Derivations. *arXiv preprint arXiv:1611.06122* **2016**,
- 674 (68) Plimpton, S. Fast parallel algorithms for short-range molecular dynamics. *Journal of
675 computational physics* **1995**, *117*, 1–19.
- 676 (69) Mattoni, A.; Filippetti, A.; Saba, M. I.; Delugas, P. Methylammonium Rotational
677 Dynamics in Lead Halide Perovskite by Classical Molecular Dynamics: The Role of
678 Temperature. *The Journal of Physical Chemistry C* **2015**, *119*, 17421–17428.
- 679 (70) Mayers, M. Z.; Tan, L. Z.; Egger, D. A.; Rappe, A. M.; Reichman, D. R. How Lattice
680 and Charge Fluctuations Control Carrier Dynamics in Halide Perovskites. *Nano Letters*
681 **2018**, *18*, 8041–8046.
- 682 (71) Milot, R. L.; Eperon, G. E.; Snaith, H. J.; Johnston, M. B.; Herz, L. M. Temperature-
683 Dependent Charge-Carrier Dynamics in CH₃NH₃PbI₃ Perovskite Thin Films. *Advanced
684 Functional Materials* **2015**, *25*, 6218–6227.

- 685 (72) Gélvez-Rueda, M. C.; Cao, D. H.; Patwardhan, S.; Renaud, N.; Stoumpos, C. C.;
686 Schatz, G. C.; Hupp, J. T.; Farha, O. K.; Savenije, T. J.; Kanatzidis, M. G.;
687 Grozema, F. C. Effect of Cation Rotation on Charge Dynamics in Hybrid Lead Halide
688 Perovskites. *The Journal of Physical Chemistry C* **2016**, *120*, 16577–16585.
- 689 (73) Guo, Z.; Manser, J. S.; Wan, Y.; Kamat, P. V.; Huang, L. Spatial and Temporal Imaging
690 of Long-Range Charge Transport in Perovskite Thin Films by Ultrafast Microscopy.
691 *Nature Communications* **2015**, *6*, 7471.
- 692 (74) Oga, H.; Saeki, A.; Ogomi, Y.; Hayase, S.; Seki, S. Improved Understanding of the
693 Electronic and Energetic Landscapes of Perovskite Solar Cells: High Local Charge
694 Carrier Mobility, Reduced Recombination, and Extremely Shallow Traps. *Journal of*
695 *the American Chemical Society* **2014**, *136*, 13818–13825.
- 696 (75) Lim, J.; T. Hörantner, M.; Sakai, N.; M. Ball, J.; Mahesh, S.; K. Noel, N.; Lin, Y.-H.;
697 B. Patel, J.; P. McMeekin, D.; B. Johnston, M.; Wenger, B.; J. Snaith, H. Elucidating
698 the Long-Range Charge Carrier Mobility in Metal Halide Perovskite Thin Films. *Energy*
699 *& Environmental Science* **2019**, *12*, 169–176.
- 700 (76) Wehrenfennig, C.; Eperon, G. E.; Johnston, M. B.; Snaith, H. J.; Herz, L. M. High
701 Charge Carrier Mobilities and Lifetimes in Organolead Trihalide Perovskites. *Advanced*
702 *Materials* **2014**, *26*, 1584–1589.
- 703 (77) Karakus, M.; Jensen, S. A.; D’Angelo, F.; Turchinovich, D.; Bonn, M.; Cánovas, E.
704 Phonon–Electron Scattering Limits Free Charge Mobility in Methylammonium Lead
705 Iodide Perovskites. *The Journal of Physical Chemistry Letters* **2015**, *6*, 4991–4996.
- 706 (78) Zhou, J.; Lei, N.; Zhou, H.; Zhang, Y.; Tang, Z.; Jiang, L. Understanding the
707 Temperature-Dependent Charge Transport, Structural Variation and Photolumines-
708 cent Properties in Methylammonium Lead Halide Perovskite Single Crystals. *Journal*
709 *of Materials Chemistry C* **2018**, *6*, 6556–6564.

- 710 (79) Shrestha, S.; Matt, G. J.; Osvet, A.; Niesner, D.; Hock, R.; Brabec, C. J. Assessing
711 Temperature Dependence of Drift Mobility in Methylammonium Lead Iodide Perovskite
712 Single Crystals. *The Journal of Physical Chemistry C* **2018**, *122*, 5935–5939.
- 713 (80) Tan, L. Z.; Zheng, F.; Rappe, A. M. Intermolecular Interactions in Hybrid Perovskites
714 Understood from a Combined Density Functional Theory and Effective Hamiltonian
715 Approach. *ACS Energy Letters* **2017**, *2*, 937–942.
- 716 (81) Li, B.; Kawakita, Y.; Liu, Y.; Wang, M.; Matsuura, M.; Shibata, K.; Ohira-
717 Kawamura, S.; Yamada, T.; Lin, S.; Nakajima, K.; Liu, S. F. Polar Rotor Scatter-
718 ing as Atomic-Level Origin of Low Mobility and Thermal Conductivity of Perovskite
719 CH₃NH₃PbI₃. *Nature Communications* **2017**, *8*, 16086.
- 720 (82) Kadanoff, L. P. Boltzmann Equation for Polarons. *Physical Review* **1963**, *130*, 1364–
721 1369.
- 722 (83) Christov, S. G. Adiabatic Polaron Theory of Electron Hopping in Crystals: A Reaction-
723 Rate Approach. *Physical Review B* **1982**, *26*, 6918–6935.